

# Fast Steerable Principal Component Analysis

Zhizhen Zhao<sup>1</sup>, Yoel Shkolnisky<sup>2</sup>, Amit Singer<sup>3</sup>

<sup>1</sup>Courant Institute of Mathematical Sciences, New York University, New York, NY, USA

<sup>2</sup>Department of Applied Mathematics, Tel Aviv University, Tel Aviv, Israel

<sup>3</sup>Program in Applied and Computational Mathematics, Princeton University, Princeton, NJ, USA

Cryo-electron microscopy nowadays often requires the analysis of hundreds of thousands of 2D images as large as a few hundred pixels in each direction. Here we introduce an algorithm that efficiently and accurately performs principal component analysis (PCA) for a large set of two-dimensional images, and, for each image, the set of its uniform rotations in the plane and their reflections. For a dataset consisting of  $n$  images of size  $L \times L$  pixels, the computational complexity of our algorithm is  $O(nL^3 + L^4)$ , while existing algorithms take  $O(nL^4)$ . The new algorithm computes the expansion coefficients of the images in a Fourier-Bessel basis efficiently using the non-uniform fast Fourier transform. We compare the accuracy and efficiency of the new algorithm with traditional PCA and existing algorithms for steerable PCA. In particular, for certain parameter values the running time of the new algorithm is 25 times faster.

*Index Terms*—Steerable PCA, group invariance, non-uniform FFT, denoising.

## I. INTRODUCTION

Principal component analysis (PCA) is widely used in image analysis and pattern recognition for dimensionality reduction and denoising. In particular, PCA is often one of the first steps [1] in the algorithmic pipeline of cryo-electron microscopy (EM) single particle reconstruction (SPR) [2] to compress and denoise the acquired 2D projection images in order to eventually determine the 3D structure of a macromolecule. As any planar rotation of any given projection image is equally likely to appear in the experiment, by either in-plane rotating the detector or the specimen, it makes sense to include all possible rotations of the projection images when performing PCA. The resulting principal components are tensor products of radial functions and angular Fourier modes [3], [4], [5], [6], [7]. Beyond cryo-EM, steerable PCA has many other applications in image analysis and computer vision [8]. The term “steerable PCA” comes from the fact that rotating the principal components is achieved by a simple phase shift of the angular part. The principal components are invariant to any in-plane rotations of the images, therefore finding steerable principal components is equivalent to finding in-plane rotationally invariant principal components. Previously, [9], [10] proposed a group theoretical framework for constructing group invariant features and filters in a Hilbert space, which is applicable to a wide range of group actions, such as those corresponding to  $SO(3)$  and  $SU(1, 1)$  [11], [12]. The representation of finite groups, such as the dihedral groups  $D(n)$ , is used for computing the Karhunen-Loève expansion of digital images [13]. In this paper, we focus on the action of the group  $O(2)$  on digital images by in-plane rotating and possibly reflecting them.

Various efficient algorithms for steerable PCA have been introduced [14], [6]. However, steerable PCA of modern cryo-EM datasets that contain hundreds of thousands of large images poses a computational challenge. Also, it is important to ensure that the algorithm is numerically accurate when

the input images are noisy. In order to exploit the special separation of variables structure of the principal components in polar coordinates, most algorithms rely on resampling the images on a polar grid. However, the transformation from Cartesian to polar is non-unitary, and thus changes the statistics of the noise. In particular, resampling transforms uncorrelated white noise to colored noise that may lead to spurious principal components.

Recently, [7] addressed this issue by incorporating a sampling criterion to the steerable PCA framework and introduced an algorithm called Fourier-Bessel steerable PCA (FBsPCA). FBsPCA assumes that the underlying clean images (before being possibly contaminated with noise) are bandlimited and essentially compactly supported in a disk. This assumption holds, for example, for 2D projection images of a 3D molecule compactly supported in a ball. This assumption implies that the images can be expanded in an orthogonal basis for the bandlimited functions, such as the Fourier-Bessel basis. In FBsPCA, the Fourier-Bessel expansion is truncated into a finite series using a sampling criterion that was introduced by Klug and Crowther [15]. The first step of FBsPCA consists of computing a truncated Fourier-Bessel expansion for each image. The sampling criterion ensures that the transformation from the Cartesian grid to the truncated Fourier-Bessel expansion is nearly unitary. Moreover, the covariance matrix built from the expansion coefficients of the images and all their possible rotations has a block diagonal structure where the block size decreases as a function of the angular frequency. The computational complexity of FBsPCA is  $O(nL^4)$  for  $n$  images of size  $L \times L$ . Notice that the computational complexity of traditional PCA is  $O(nL^4 + L^6)$  where the first term corresponds to forming the  $L^2 \times L^2$  covariance matrix and the second term corresponds to its eigen-decomposition. FBsPCA is thus more efficient than traditional PCA, and it also leads to better denoising as it takes into account also possible rotations and reflections. These properties make FBsPCA more suitable than traditional PCA as a tool for 2D analysis of cryo-EM images [7]. With the enhancement of electron microscope

detector resolution, a typical image size of a single particle can easily be over  $300 \times 300$  pixels. Yet, FFBsPCA is still not efficient enough to analyze a large number of images of large size (i.e. large  $n$  and large  $L$ ). The bottleneck for this algorithm is the first step that computes the Fourier-Bessel expansion coefficients, whose computational complexity is  $O(nL^4)$ .

In this paper we introduce a fast Fourier-Bessel steerable PCA (FFBsPCA) that reduces the computational complexity for FFBsPCA by computing the Fourier-Bessel expansion coefficients more efficiently. This is achieved by first mapping the images from their Cartesian grid representation to a polar grid representation in the reciprocal (Fourier) domain using the non-uniform fast Fourier transform (NUFFT) [16], [17], [18], [19]. The radius of the disk is determined by the band limit of the images. The polar grid representation enables a faster computation of the Fourier-Bessel expansion coefficients. The expansion coefficients of the images are efficiently evaluated by 1D FFT on concentric rings followed by accurate evaluation of a radial integral with a Gaussian quadrature rule. The overall complexity of computing the Fourier-Bessel coefficients is reduced to  $O(nL^3)$ , which serves as the main contribution of this paper.

We note that the expansion coefficients can be computed in  $O(nL^2 \log(L))$  using algorithms for rapid evaluation of special functions [20] or a fast analysis-based Fourier-Bessel expansion [21]. However, such “fast” algorithms may only lead to marginal improvement for two reasons. First, the break even point for them compared to the direct approach is for relatively large  $L$  such as  $L = 256$  or larger. Second, forming the covariance matrix from the expansion coefficients still requires  $O(nL^3)$  operations.

The paper is organized as follows: Section II contains the mathematical preliminaries of the Fourier-Bessel expansion, the sampling criterion, and the numerical evaluation of the expansion coefficients. The computation of the steerable principal components is described in Section III. We present the algorithm and give a detailed computational complexity analysis in Section IV. Various numerical examples concerning the computation time of FFBsPCA compared with FBsPCA and traditional PCA are presented in Section V. In the same section, we demonstrate the denoising effects on simulated cryo-EM projection images.

**Reproducible research:** The FFBsPCA is available in the SPR toolbox ASPIRE (<http://spr.math.princeton.edu/>). There are two main functions: *FBCoeff* computes the Fourier Bessel expansion coefficients and *sPCA* computes the steerable PCA basis and the associated expansion coefficients.

## II. FOURIER-BESSEL EXPANSION OF BANDLIMITED IMAGES

All digital images are essentially bandlimited. In our setup, a digital image  $I$  is obtained by sampling a squared-integrable bandlimited function  $f$  on a Cartesian grid of size  $L \times L$ ,

$$I(i_1, i_2) = f(i_1 \Delta, i_2 \Delta), \quad (1)$$

for  $i_1, i_2 = -\lceil \frac{L-1}{2} \rceil, \dots, \lfloor \frac{L-1}{2} \rfloor$ , where  $\Delta$  is the pixel size.

We say that  $f$  has a band limit radius  $c$  if its Fourier transform

$$\mathcal{F}(f)(\xi_1, \xi_2) = \int_{\mathbb{R}^2} f(x, y) e^{-2\pi i(x\xi_1 + y\xi_2)} dx dy \quad (2)$$

satisfies

$$\mathcal{F}(f)(\xi_1, \xi_2) = 0, \quad \text{for } \xi_1^2 + \xi_2^2 > c^2. \quad (3)$$

From the Fourier inversion formula

$$f(x, y) = \int_{\xi_1^2 + \xi_2^2 \leq c^2} \mathcal{F}(f)(\xi_1, \xi_2) e^{2\pi i(x\xi_1 + y\xi_2)} d\xi_1 d\xi_2. \quad (4)$$

For pixel size  $\Delta = 1$ , the Nyquist-Shannon sampling theorem implies that the Fourier transform is supported on the square  $(-1/2, 1/2] \times (-1/2, 1/2]$ . In many applications, the support size is effectively smaller due to other experimental considerations, such as the exponentially decaying envelope of the contrast transfer function in electron microscopy. We assume that the band limit radius of all images is  $0 < c \leq \frac{1}{2}$ . The scaled Fourier-Bessel functions are the eigenfunctions of the Laplacian in a disk of radius  $c$  with Dirichlet boundary condition and they are given by

$$\psi_c^{k,q}(\xi, \theta) = \begin{cases} N_{k,q} J_k \left( R_{k,q} \frac{\xi}{c} \right) e^{ik\theta}, & \xi \leq c, \\ 0, & \xi > c, \end{cases} \quad (5)$$

where  $(\xi, \theta)$  are polar coordinates in the Fourier domain (i.e.,  $\xi_1 = \xi \cos \theta$ ,  $\xi_2 = \xi \sin \theta$ ,  $\xi \geq 0$ , and  $\theta \in [0, 2\pi)$ );  $N_{k,q} = (c\sqrt{\pi} |J_{k+1}(R_{k,q})|)^{-1}$  is the normalization factor;  $J_k$  is the Bessel function of the first kind of integer order  $k$ ; and  $R_{k,q}$  is the  $q^{\text{th}}$  root of the Bessel function  $J_k$ . For a function  $f$  with band limit  $c$  that is also in  $L^2(\mathbb{R}^2) \cap L^1(\mathbb{R}^1)$ ,

$$\mathcal{F}(f)(\xi, \theta) = \sum_{k=-\infty}^{\infty} \sum_{q=1}^{\infty} a_{k,q} \psi_c^{k,q}(\xi, \theta), \quad (6)$$

and the Fourier-Bessel expansion converges pointwise. In Section II-A, we derive a finite truncation rule for the Fourier-Bessel expansion in Eq. (6).

### A. Sampling criterion

We assume the underlying clean images (before being possibly contaminated with noise) are essentially compactly supported in a disk of radius  $R$ . The infinite Fourier-Bessel expansion as in Eq. (6) is not feasible computationally and also introduces spurious information from noise. Therefore, we would like to employ a sampling criterion for selecting  $k$  and  $q$  so that Eq. (6) becomes a finite expansion.

With the following convention for the 2D inverse polar Fourier transform of a function  $g(\xi, \theta)$ ,

$$\mathcal{F}^{-1}(g)(r, \phi) = \int_0^{2\pi} \int_0^\infty g(\xi, \theta) e^{2\pi i r \xi \cos(\theta - \phi)} \xi d\xi d\theta, \quad (7)$$

the 2D inverse Fourier transform of the Fourier-Bessel functions, denoted  $\mathcal{F}^{-1}(\psi_c^{k,q})$ , is given in polar coordinates as

$$\mathcal{F}^{-1}(\psi_c^{k,q})(r, \phi) = \frac{2c\sqrt{\pi}(-1)^q R_{k,q} J_k(2\pi cr)}{i^k((2\pi cr)^2 - R_{k,q}^2)} e^{ik\phi}. \quad (8)$$

The maximum of  $|\mathcal{F}^{-1}(\psi_c^{k,q})(r, \phi)|$  in (8) is obtained near the ring  $r = \frac{R_{k,q}}{2\pi c}$  and  $\mathcal{F}^{-1}(\psi_c^{k,q})(r, \phi)$  vanishes on concentric rings of radii  $r = \frac{R_{k,q'}}{2\pi c}$  with  $q' \neq q$ . The smallest ring with vanishing  $\mathcal{F}^{-1}(\psi_c^{k,q})$  that encircles the maximum of  $|\mathcal{F}^{-1}(\psi_c^{k,q})|$  is of radius  $r = \frac{R_{k,(q+1)}}{2\pi c}$ .

Since the images are assumed to be essentially compactly supported, we should rule out Fourier-Bessel functions for which the maximum of their inverse Fourier transform resides outside a disk of radius  $R$ . Notice that if the maximum is inside the disk, yet the zero after the maximum is outside the disk, then there is a significant spillover of energy outside the disk. We therefore require the more stringent criterion that the zero after the maximum is inside the disk, namely

$$\frac{R_{k,(q+1)}}{2\pi c} \leq R. \quad (9)$$

The sampling argument gives a finite truncation rule for the Fourier-Bessel expansion in Eq. (6), that is

$$R_{k,(q+1)} \leq 2\pi c R. \quad (10)$$

For each  $k$ , we denote by  $p_k$  the number of components satisfying Eq. (10). We also denote by  $p = \sum_{k=-k_{\max}}^{k_{\max}} p_k$  the total number of components. The positions of Bessel zeros have been extensively studied, for example, in [22, p.517-521][23, p.370][24], [25], [26]. Several lower and upper bounds for Bessel zeros  $R_{k,q}$  were proven by Breen in [26], such as

$$R_{k,q} > k + \frac{2}{3}|a_{q-1}|^{3/2}, \quad (11)$$

where  $a_q$  is the  $q$ th zero of the Airy function. Breen also provided the following upper and lower bounds for  $a_q$ ,

$$\left[ \frac{3}{8}\pi(4q - 1.4) \right]^{2/3} < |a_q| < \left[ \frac{3}{8}\pi(4q - 0.965) \right]^{2/3}. \quad (12)$$

Using the lower bound for  $|a_q|$  and the sampling criterion in Eq. (10), we have the following inequality for  $k$  and  $p_k$ ,

$$2\pi c R \approx R_{k,p_k+1} > k + \pi p_k - \frac{1.4\pi}{4}. \quad (13)$$

Breen also obtained

$$R_{k,q} < \left( \frac{k}{2} + q - \frac{0.965}{4} \right) \pi, \quad (14)$$

so we get another inequality for  $k$  and  $p_k$ ,

$$2\pi c R \approx R_{k,p_k+1} < \left( \frac{k}{2} + p_k + \frac{3.035}{4} \right) \pi. \quad (15)$$

Combining Eqs. (13) and (15), we have the following lower and upper bounds for  $p_k$ ,

$$2cR - \frac{k}{2} - \frac{3.035}{4} < p_k < 2cR - \frac{k}{\pi} + \frac{1.4}{4}. \quad (16)$$

The maximum angular frequency  $k_{\max}$  occurs when  $p_k = 1$ , and therefore

$$4cR - 3.517 < k_{\max} < 2\pi c R - 2.042. \quad (17)$$

Equation (16) implies that as the angular frequency  $k$  increases, the number of components  $p_k$  decreases. Moreover, using the lower and upper bounds for  $p_k$  and  $k_{\max}$  in Eqs. (16)

and (17), we derive that the total number of selected Fourier-Bessel basis functions is between  $8(cR)^2$  and  $4\pi(cR)^2$ . When  $c$  is the largest band limit, i.e.  $c = \frac{1}{2}$ , the number of basis functions is between  $2R^2$  and  $\pi R^2$ , where the latter is approximately the number of pixels inside the unit disk of radius  $R$ . Also, whenever  $c = O(1)$  and  $R = O(L)$ , then  $p = O(L^2)$  and  $k_{\max} = O(L)$ .

Because the bandlimited function  $f$  is assumed to be essentially compactly supported, the infinite expansion in Eq. (6) is approximated by the finite expansion

$$P_{c,R}\mathcal{F}(f)(\xi, \theta) = \sum_{k=-k_{\max}}^{k_{\max}} \sum_{q=1}^{p_k} a_{k,q} \psi_c^{k,q}(\xi, \theta), \quad (18)$$

where  $P_{c,R}$  is the orthogonal projection from  $L^2(D_c)$  (the space of  $L^2$  functions supported on a disk of radius  $c$ ), to the space of functions spanned by a finite number of Fourier-Bessel functions that satisfy (10).

### B. Numerical Evaluation of Fourier-Bessel Expansion Coefficients

Previously in [7], the evaluation of the expansion coefficients  $a_{k,q}$  was done by least squares. Let  $\Psi$  be the matrix whose entries are evaluations of the Fourier-Bessel functions at the Cartesian grid points, with rows indexed by the grid points and columns indexed by angular and radial frequencies. Finding the coefficient vector  $a$  as the solution to  $\min_a \|\Psi a - I\|_2^2$  requires the computation of  $\Psi^* I$ , which takes  $O(pL^2) = O(L^4)$  operations, because  $p = O(L^2)$ . In general  $a = (\Psi^* \Psi)^{-1} \Psi^* I$ , but here  $\Psi^* \Psi$  is approximately the identity matrix, due to the orthogonality of the Fourier-Bessel functions.

We introduce here a method that computes the expansion coefficients in  $O(L^3)$  instead of  $O(L^4)$ . We first evaluate the Fourier coefficients on a polar grid, which is an instance of a nonuniform discrete Fourier transform, defined as

$$F(I)(\xi_1, \xi_2) = \frac{1}{(2R)^2} \sum_{i_1=-R}^{R-1} \sum_{i_2=-R}^{R-1} I(i_1, i_2) e^{-i2\pi(\xi_1 i_1 + \xi_2 i_2)}, \quad (19)$$

where  $-1/2 \leq \xi_1, \xi_2 \leq 1/2$ . For the polar grid,  $\xi_1(j, l) = \xi_j \cos(2\pi l/n_\theta)$ ,  $\xi_2(j, l) = \xi_j \sin(2\pi l/n_\theta)$ ,  $j = 1, \dots, n_\xi$ ,  $l = 0, \dots, n_\theta - 1$ . The angles are sampled uniformly on each concentric ring of radius  $\xi_j$ . The radius of each concentric ring  $\xi_j$  is determined by a Gaussian quadrature rule, and thus the sample points on each radial line are not equally spaced (see Fig. 1). The choice of  $n_\xi$  and  $n_\theta$  depends on the compact support radius  $R$  and band limit  $c$  and is derived later in the paper.

The expansion coefficients in Eq. (18) are given by

$$\begin{aligned} a_{k,q} &= \int_0^{2\pi} \int_0^c \mathcal{F}(f)(\xi, \theta) \overline{\psi_c^{k,q}(\xi, \theta)} \xi d\xi d\theta \\ &= \int_0^c N_{k,q} J_k \left( R_{k,q} \frac{\xi}{c} \right) \xi d\xi \int_0^{2\pi} \mathcal{F}(f)(\xi, \theta) e^{-ik\theta} d\theta, \end{aligned} \quad (20)$$

where  $f$  is the bandlimited function whose samples form the digital image  $I$ . The integral in Eq. (20) can be numerically

evaluated using discrete samples on a polar Fourier grid. The angular integration is sped up by 1D FFT on the concentric circles and it is followed by a numerical evaluation of the radial integral with a Gaussian quadrature rule. As the samples on each concentric circle are uniform, the natural quadrature weight for the angular integral is  $\frac{2\pi}{n_\theta}$  and the points are taken at  $\theta_l = \frac{2\pi l}{n_\theta}$  for  $l = 0, \dots, n_\theta - 1$ . The angular integration using one-dimensional FFT on each concentric ring thus yields

$$\widehat{F(I)}(\xi_j, k) = \frac{2\pi}{n_\theta} \sum_{l=0}^{n_\theta-1} F(I)(\xi_j, \theta_l) e^{-i \frac{2\pi k l}{n_\theta}}. \quad (21)$$

The radial integral is evaluated using the Gauss-Legendre quadrature rule [27, Chap. 4], which determines the locations of  $n_\xi$  points  $\{\xi_j\}_{j=1}^{n_\xi}$  on the interval  $[0, c]$  and the associated weights  $w(\xi_j)$ . The integral in Eq. (20) is thus approximated by

$$a_{k,q} \approx \sum_{j=1}^{n_\xi} N_{k,q} J_k \left( R_{k,q} \frac{\xi_j}{c} \right) \widehat{F(I)}(\xi_j, k) \xi_j w(\xi_j). \quad (22)$$

The procedure for numerical evaluation of the Fourier-Bessel expansion coefficients is illustrated in Fig. 1. In practice, we have observed that sampling with  $n_\xi = 4cR$  and  $n_\theta = 16cR$  gives numerical evaluation of the integral in Eq. 20 with high accuracy.

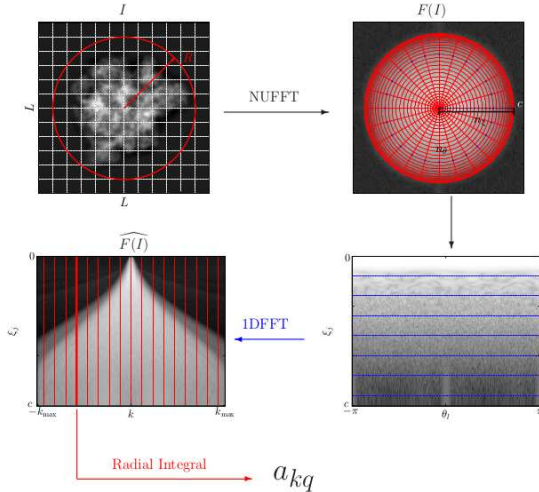


Fig. 1: Pictorial summary of the procedure for computing the Fourier-Bessel expansion coefficients. The original image (top left) is resampled on a polar Fourier grid (Eq. (19)) using NUFFT (top right and bottom right) followed by 1D FFT (Eq. (21)) on each concentric ring. The evaluation of the radial integral (Eq. (22)) gives the expansion coefficients  $a_{k,q}$ . The bow-tie phenomenon illustrated in bottom-left was discussed in [28].

If our signal can be expressed in terms of the truncated Fourier-Bessel expansion in Eq. (18), the approximation error in the radial integral comes from the numerical evaluation of the integrals

$$G(k, q_1, q_2) = \int_0^c J_k \left( R_{k,q_1} \frac{\xi}{c} \right) J_k \left( R_{k,q_2} \frac{\xi}{c} \right) \xi d\xi, \quad (23)$$

The approximation error using  $n_\xi$  discrete samples is

$$E(k, q_1, q_2; n_\xi) = \left| \sum_{j=1}^{n_\xi} J_k \left( R_{k,q_1} \frac{\xi_j}{c} \right) J_k \left( R_{k,q_2} \frac{\xi_j}{c} \right) \xi_j w(\xi_j) - G(k, q_1, q_2) \right| \quad (24)$$

Asymptotically, a Bessel function behaves like a decaying cosine function with frequency  $\frac{R_{k,q}}{2\pi}$  for  $R_{k,q}r \gg |k^2 - \frac{1}{4}|$  [23],

$$J_k(R_{k,q}r) \sim \sqrt{\frac{2}{\pi R_{k,q}r}} \cos(R_{k,q}r - \frac{k\pi}{2} - \frac{\pi}{4}). \quad (25)$$

For a fixed  $n_\xi$ , the largest approximation error occurs when  $k = 0$  and  $q_1 = q_2 = p_0$ , since  $J_0 \left( R_{0,p_0} \frac{\xi}{c} \right)$  is the most oscillatory function within the band limit. The Nyquist rate of  $\xi J_0^2 \left( R_{0,p_0} \frac{\xi}{c} \right)$  is  $2 \frac{2R_{0,p_0}}{2\pi} \approx 4cR$  and we need to sample at Nyquist rate, or higher. Therefore, we choose  $n_\xi = \lceil 4cR \rceil$ . Fig. 2a justifies this choice as the error decays dramatically to  $10^{-17}$  before  $n_\xi = \lceil 4cR \rceil$ .

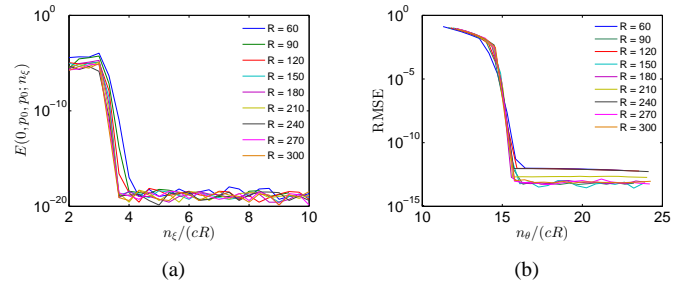


Fig. 2: (a) Error, as a function of  $n_\xi$ , in the numerical evaluation of the integral in  $G(0, p_0, p_0)$  Eq. (23). (b) Error, as a function of  $n_\theta$ , in the evaluation of the integral in Eq. (20).

To choose  $n_\theta$ , we computed the root mean squared error (RMSE) in evaluating the expansion coefficients for simulated images composed of white Gaussian noise with various  $R$  and  $n_\theta$ , while  $c = 1/2$ . We oversampled on the radial lines by  $n_\xi = \lceil 10cR \rceil$  and the ground truth is computed via oversampling in the angular direction by  $n_\theta = 60cR$ . We observe that when  $n_\theta \geq 16cR$ , the estimation error becomes negligible (see Fig. 2b). Notice that Eq. (17) implies that  $k_{\max} < 2\pi cR$ . The corresponding Nyquist rate is bounded by  $4\pi cR$ . We therefore sample at a slightly higher rate  $n_\theta = 16cR$  to ensure numerical accuracy.

Now that we are able to numerically evaluate  $a_{k,q}$  with high accuracy, we can study the spectral behavior of the finite Fourier-Bessel expansion of the images. We define  $a$  as the vector that contains the expansion coefficients  $a_{k,q}$  computed in (22) and use  $T^*$  to denote the transformation that maps an image sampled on a Cartesian grid to the finite Fourier-Bessel expansion coefficients through Eqs. (19), (21) and (22), that is,

$$a = T^* I. \quad (26)$$

Ideally we would like  $T^*$  to be a unitary transformation, that is,  $T^* T = I$  so that the transformation from the images to

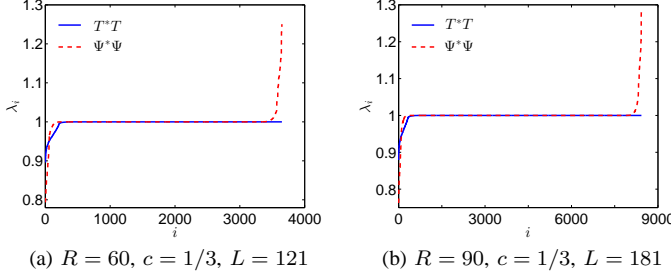


Fig. 3: Eigenvalues of  $T^*T$  and  $\Psi^*\Psi$ , where  $T^*$  and  $\Psi^*$  are the truncated Fourier-Bessel transform using numerical integration and least squares respectively. These are also the spectra of the population covariance matrices of transformed white noise images. Most eigenvalues are close to 1, indicating that the truncated Fourier-Bessel transform is almost unitary. Thus white noise remains approximately white.

the coefficients preserves the noise statistics. Numerically, we observe that the majority of the eigenvalues of  $T^*T$  are 1 and the smallest eigenvalues are also close to 1 (see blue line in Fig. 3). The transformation  $T^*$  is close to unitary because it is a numerical approximation of an expansion in an orthogonal basis (Fourier-Bessel), and the sampling criterion prevents aliasing. In Fig. 3, the eigenvalues of  $\Psi^*\Psi$  are also plotted for comparison.  $T^*T$  has fewer eigenvalues that deviate from 1. Although the Fourier-Bessel functions are orthogonal as continuous functions, their discrete sampled versions are not necessarily orthogonal, hence  $\Psi^*\Psi$  deviates from the identity matrix. The fact that  $T^*T$  is closer to the identity than  $\Psi^*\Psi$  implies that the numerical evaluation of the expansion coefficient vector  $a$  as  $T^*I$  is more accurate than estimating it as  $\Psi^*I$ .

Computing the polar Fourier transform of an image of size  $L \times L$  on a polar grid with  $n_\xi \times n_\theta$  points in Eq. (19) is implemented efficiently using NUFFT [16], [17], [18], [19], whose computational complexity is  $O(L^2 \log L + n_\xi n_\theta)$ . Since  $n_\theta = 16cR = O(L)$  and  $n_\xi = 4cR = O(L)$ ,  $n_\xi \times n_\theta = O(L^2)$  and the complexity of the discrete polar Fourier transform is  $O(L^2 \log L)$ . The complexity of the 1D FFTs in Eq. (21) is  $O(n_\xi n_\theta \log n_\theta)$ , because there are  $n_\xi$  concentric circles with  $n_\theta$  samples on each circle. Both  $n_\xi$  and  $n_\theta$  are of  $O(L)$ , so the total complexity of the 1D FFTs is also  $O(L^2 \log L)$ . The radial integral using the quadrature rule in Eq. (20) has computational complexity of  $O(L^3)$  using a direct method, because there are  $O(L^2)$  basis functions and each radial function has  $O(L)$  sample points. However, this complexity can be reduced to  $O(L^2 \log L)$  using a fast Bessel transform [20], [21]. In summary, the computational complexity for computing the Fourier-Bessel expansion coefficients of an image of size  $L \times L$  is  $O(L^3)$ , or  $O(L^2 \log L)$  using a “fast” transform.

### III. SAMPLE COVARIANCE MATRIX

Given a dataset of  $n$  images  $\{I_i\}_{i=1}^n$ , we denote by  $f_i$  the underlying bandlimited function that corresponds to the  $i$ 'th image  $I_i$ . Under the action of the group  $O(2)$ , the function

$f_i$  is transformed to  $f_i^{\alpha,\beta}$ , where  $\alpha \in [0, 2\pi)$  is the counter-clockwise rotational angle and  $\beta$  denotes reflection and takes values in  $\{+, -\}$ . More specifically,  $f_i^{\alpha,+}(r, \phi) = f_i(r, \phi - \alpha)$  and  $f_i^{\alpha,-}(r, \phi) = f_i(r, \pi - (\phi - \alpha))$ . The images  $I_i^{\alpha,+}$  and  $I_i^{\alpha,-}$  are obtained by sampling  $f_i^{\alpha,+}$  and  $f_i^{\alpha,-}$  respectively.

The Fourier transform of  $f_i$  commutes with the action of the group  $O(2)$ , namely,  $\mathcal{F}(f_i^{\alpha,+})(\xi, \theta) = \mathcal{F}(f_i)^{\alpha,+}(\xi, \theta) = \mathcal{F}(f_i)(\xi, \theta - \alpha)$ , and  $\mathcal{F}(f_i^{\alpha,-})(\xi, \theta) = \mathcal{F}(f_i)^{\alpha,-}(\xi, \theta) = \mathcal{F}(f_i)(\xi, \pi - (\theta - \alpha))$ . Since  $\mathcal{F}(f_i)$  is well-approximated by  $P_{c,R}\mathcal{F}(f_i)$ , the transformation of the images under rotation and reflection can be easily represented by the transformation of the truncated expansion coefficients in terms of the Fourier-Bessel basis. Under counter-clockwise rotation by an angle  $\alpha$ ,  $P_{c,R}\mathcal{F}(f_i^{\alpha,+})$ , is given by

$$\begin{aligned} P_{c,R}\mathcal{F}(f_i^{\alpha,+})(\xi, \theta) &= \sum_{k,q} a_{k,q}^i \psi_c^{k,q}(\xi, \theta - \alpha) \\ &= \sum_{k,q} a_{k,q}^i e^{-ik\alpha} \psi_c^{k,q}(\xi, \theta). \end{aligned} \quad (27)$$

Therefore the planar rotation introduces a phase shift in the expansion coefficients. Under rotation and reflection,

$$\begin{aligned} P_{c,R}\mathcal{F}(f_i^{\alpha,-})(\xi, \theta) &= \sum_{k,q} a_{k,q}^i \psi_c^{k,q}(\xi, \pi - (\theta - \alpha)) \\ &= \sum_{k,q} a_{k,q}^i N_{k,q} J_k \left( R_{k,q} \frac{\xi}{c} \right) e^{ik(\pi - \theta + \alpha)} \\ &= \sum_{k,q} a_{k,q}^i N_{k,q} (-1)^k J_k \left( R_{k,q} \frac{\xi}{c} \right) e^{i(-k)\theta} e^{ik\alpha} \\ &= \sum_{k,q} a_{k,q}^i e^{ik\alpha} \psi_c^{-k,q}(\xi, \theta) = \sum_{k,q} a_{-k,q}^i e^{-ik\alpha} \psi_c^{k,q}(\xi, \theta), \end{aligned} \quad (28)$$

namely, the expansion coefficient  $a_{k,q}^i$  changes to  $a_{-k,q}^i e^{-ik\alpha}$ .

If we augment the collection of the bandlimited functions  $\{f_i\}_{i=1}^n$  by all possible rotations and reflections, the Fourier transform of the sample mean  $f_{\text{mean}}$  becomes,

$$\mathcal{F}(f_{\text{mean}})(\xi, \theta) = \frac{1}{2n} \sum_{i=1}^n \sum_{\beta \in \{+, -\}} \frac{1}{2\pi} \int_0^{2\pi} \mathcal{F}(f_i^{\alpha,\beta})(\xi, \theta) d\alpha. \quad (29)$$

Since  $f_{\text{mean}}$  is also a bandlimited function that is essentially compactly supported within radius  $R$ ,  $\mathcal{F}(f_{\text{mean}})$  can be well-approximated by  $P_{c,R}\mathcal{F}(f_{\text{mean}})$ , the finite dimensional Fourier-Bessel expansion. Using the properties in Eqs. (27) and (28), we have

$$\begin{aligned} P_{c,R}\mathcal{F}(f_{\text{mean}})(\xi, \theta) &= \frac{1}{2n} \sum_{i=1}^n \frac{1}{2\pi} \\ &\times \int_0^{2\pi} \sum_{k=-k_{\max}}^{k_{\max}} \sum_{q=1}^{p_k} [a_{k,q}^i + a_{-k,q}^i] e^{-ik\alpha} \psi_c^{k,q}(\xi, \theta) d\alpha \\ &= \sum_{q=1}^{p_0} \left( \frac{1}{n} \sum_{i=1}^n a_{0,q}^i \right) \psi_c^{0,q}(\xi, \theta). \end{aligned} \quad (30)$$

As expected, the sample mean is radially symmetric, because  $\psi_c^{0,q}$  is only a function of  $\xi$  but not of  $\theta$ .

The rotationally invariant covariance kernel  $\mathcal{C}((\xi, \theta), (\xi', \theta'))$  built from Fourier transformed functions with all their possible in-plane rotations and reflections is defined as

$$\mathcal{C}((\xi, \theta), (\xi', \theta')) = \frac{1}{4\pi n} \sum_{i=1}^n \sum_{\beta \in \{+, -\}} \int_0^{2\pi} \left( \mathcal{F}(f_i^{\alpha, \beta})(\xi, \theta) - \mathcal{F}(f_{\text{mean}})(\xi, \theta) \right) \times \overline{\left( \mathcal{F}(f_i^{\alpha, \beta})(\xi', \theta') - \mathcal{F}(f_{\text{mean}})(\xi', \theta') \right)} d\alpha. \quad (31)$$

The kernel  $\mathcal{C}$  can be directly computed from the coefficients  $a_{k,q}^i$  using the finite expansion in the Fourier-Bessel basis and therefore it has a finite matrix representation. Subtracting the mean image is equivalent to subtracting  $\frac{1}{n} \sum_{j=1}^n a_{0,q}^j$  from the coefficients  $a_{0,q}^i$ , while keeping other coefficients unchanged. Therefore, we first update the zero angular frequency coefficients by  $a_{0,q}^i \leftarrow a_{0,q}^i - \frac{1}{n} \sum_{j=1}^n a_{0,q}^j$ , and so the finite matrix representation  $C$  of  $\mathcal{C}$  is given by

$$\begin{aligned} C_{(k,q),(k',q')} &= \frac{1}{2n} \sum_{i=1}^n \frac{1}{2\pi} \int_0^{2\pi} \left( a_{k,q}^i \overline{a_{k',q'}^i} + a_{-k,q}^i \overline{a_{-k',q'}^i} \right) e^{-i(k-k')\alpha} d\alpha \\ &= \delta_{k,k'} \frac{1}{2n} \sum_{i=1}^n \left( a_{k,q}^i \overline{a_{k',q'}^i} + a_{-k,q}^i \overline{a_{-k',q'}^i} \right), \end{aligned} \quad (32)$$

where  $\delta_{k,k'}$  comes from the integral over  $\alpha \in [0, 2\pi)$ . The covariance matrix in Eq. (32) is a block diagonal matrix because the non-zero entries of  $C$  correspond only to  $k = k'$ . Moreover, it suffices to consider  $k \geq 0$ , because  $C_{(k,q),(k',q')} = C_{(-k,q),(-k',q')}$ . Thus, the covariance matrix can be written as the direct sum  $C = \bigoplus_{k=0}^{k_{\max}} C^{(k)}$ , where  $C^{(k)}$  is by itself a sample covariance matrix of size  $p_k \times p_k$ ,

$$C_{q,q'}^{(k)} = \frac{1}{2n} \sum_{i=1}^n \left( a_{k,q}^i \overline{a_{k',q'}^i} + a_{-k,q}^i \overline{a_{-k',q'}^i} \right). \quad (33)$$

Let us denote by  $A^{(k)}$  the matrix of expansion coefficients, obtained by putting the coefficients  $a_{k,q}^i$  and  $a_{-k,q}^i$  for all  $q$ 's and all images into a matrix, where the columns are indexed by image number for both  $k$  and  $-k$  and the rows are indexed by radial indices  $q$ . The coefficient matrix for  $k \neq 0$  is of size  $p_k \times 2n$  and the covariance matrix for  $k \neq 0$  is,

$$C^{(k)} = \frac{1}{2n} A^{(k)} (A^{(k)})^*, \quad (34)$$

where  $A^*$  is the conjugate transpose ( $A_{ij}^* = \bar{A}_{ji}$ ). The case  $k = 0$  is special because the expansion coefficients satisfy  $a_{0,q} = a_{-0,q}$ , and so  $A^{(0)}$  is a matrix of size  $p_0 \times n$  and

$$C^{(0)} = \frac{1}{n} A^{(0)} (A^{(0)})^*. \quad (35)$$

The computational complexity for forming the matrix  $C^{(k)}$  is  $O(np_k^2)$ . The complexity for eigendecomposition of  $C^{(k)}$  is  $O(p_k^3)$ , since the size of the covariance matrix is  $p_k \times p_k$ . Using the upper and lower bounds for  $p_k$  in Eq. (16) and assuming  $c = O(1)$  and  $R = O(L)$ , we get  $\sum_k p_k^2 = O(L^3)$  and  $\sum_k p_k^3 = O(L^4)$ . Therefore, the complexity for forming

the covariance matrix  $C$  is  $O(n \sum_k p_k^2) = O(nL^3)$  and the complexity of the full eigendecomposition is  $O(\sum_k p_k^3) = O(L^4)$ . Equations (34) and (35) show that instead of constructing the covariance matrices  $C^{(k)}$  to compute the principal components, we can perform singular value decomposition (SVD) on the coefficient matrix  $A^{(k)}$  directly and take the left singular vectors as the principal components. The computational complexity for full rank SVD on  $A^{(k)}$  is  $O(np_k^2)$  and the total complexity of SVD of all coefficient matrices is  $O(n \sum_k p_k^2) = O(nL^3)$ .

#### IV. ALGORITHM AND COMPUTATIONAL COMPLEXITY

The new algorithm introduced in this paper is termed fast Fourier-Bessel steerable PCA (FFBsPCA). The algorithm is composed of two steps. In the first step, Fourier-Bessel expansion coefficients are computed according to Algorithm 1. The input to the algorithm includes an image dataset, the band limit  $c$ , and the compact support radius  $R$ . The second step (Algorithm 2) takes the Fourier-Bessel expansion coefficients from Algorithm 1 as input and computes the steerable PCA radial functions and the expansion coefficients of the images in the new steerable basis.

---

##### Algorithm 1: Fast Fourier-Bessel Expansion

---

- Require:**  $n$  images  $I_1, \dots, I_n$  sampled on a Cartesian grid of size  $L \times L$  with compact support radius  $R$  and band limit  $c$ .
- 1: (Precomputation) Select  $(k, q)$ 's that satisfy the sampling criterion (10). Fix  $n_\xi = 4cR$  and  $n_\theta = 16cR$ .
  - 2: (Precomputation) Find  $n_\xi$  Gaussian quadrature points and weights on the interval  $[0, c]$  and evaluate  $N_{k,q} J_k(R_{k,q} \frac{\xi_j}{c})$ ,  $j = 1, \dots, n_\xi$ , for all selected  $(k, q)$ 's.
  - 3: Compute  $F(I_i)$  (Eq. (19)) on a polar grid of size  $n_\xi \times n_\theta$  by NUFFT for each  $i = 1, \dots, n$ .
  - 4: For each  $F(I_i)$ , compute  $a_{k,q}^i$  using eqs. (21) and (22).
- 

---

##### Algorithm 2: Steerable PCA

---

- Require:** Fourier-Bessel expansion coefficients  $a_{k,q}^i$  for  $n$  images and the maximum angular frequency  $k_{\max}$ .
- 1: Compute the coefficient vector of the mean image  $a_{0,q}^{\text{mean}} = \frac{1}{n} \sum_j a_{0,q}^j$ . Then,  $a_{0,q}^i \leftarrow a_{0,q}^i - a_{0,q}^{\text{mean}}$ .
  - 2: **for**  $k = 0, 1, \dots, k_{\max}$  **do**
  - 3:   Construct coefficient matrix  $A^{(k)}$ .
  - 4:   Compute the covariance matrix  $C^{(k)}$ , its eigenvalues  $\lambda_1^{(k)} \geq \lambda_2^{(k)} \dots \geq \lambda_{p_k}^{(k)}$ , and eigenvectors,  $u_1^k, \dots, u_{p_k}^k$ ; or perform SVD of  $A^{(k)}$  and take the left singular vectors  $u_1^k, \dots, u_{p_k}^k$ .
  - 5:   Compute the radial eigenvectors as linear combinations of the normalized Bessel functions by  $f^{k,l}(\xi) = \sum_q N_{k,q} J_k(R_{k,q} \frac{\xi}{c}) u_l^k(q)$ .
  - 6:   Compute the expansion coefficients of the images in the new steerable basis by  $c_{k,l}^i = \sum_q a_{k,q}^i u_l^k(q)$ .
  - 7: **end for**
-

The computational complexity for traditional PCA, without taking into account all rotations and reflections is  $O(nL^4 + L^6)$ . It takes  $O(nL^4)$  to construct the covariance matrix and the complexity for eigendecomposition is  $O(L^6)$ . The complexity of FBsPCA introduced in [7] is  $O(nL^4)$ . The complexity of FFBsPCA is  $O(nL^3 + L^4)$ . As a result, FFBsPCA is faster than FBsPCA for large  $L$ .

The analysis of the computational complexity for FFBsPCA is as follows. The precomputation that generates all radial basis functions is  $O(L^3)$  because there are  $O(L^2)$  basis functions, each of which is sampled over  $O(L)$  points. Computing the Fourier-Bessel expansion coefficients  $a_{k,q}^i$  in Eqs. (19), (21), and (22) for all images takes  $O(nL^3)$  (or  $O(nL^2 \log L)$  with a fast Bessel transform) as discussed in Section II-B.

The complexity for constructing the covariance matrix  $C$  and computing its full eigendecomposition is  $O(nL^3 + L^4)$  as described in Section III. Another method for computing the principal components is by SVD of the coefficient matrices. Full rank SVD on all coefficient matrices requires  $O(nL^3)$  floating point operations (see Section III).

To generate the new steerable basis, we take the linear combinations of the Fourier-Bessel radial basis as in line 5 of Algorithm 2, which takes  $O(L^4)$  operations. Computing the expansion coefficients of the images in the new steerable radial basis requires  $O(nL^3)$  by taking the linear combinations of the Fourier-Bessel expansion coefficients (see line 6 in Algorithm 2). Therefore, the total computational complexity for computing steerable principal components and the associated expansion coefficients is  $O(nL^3 + L^4)$ .

FFBsPCA is easily adapted for parallel computation. The computation of Fourier-Bessel expansion coefficients in Algorithm 1 can run on multiple workers in parallel, where each worker is allocated with a subset of the images and Fourier-Bessel radial basis. Suppose each worker computes the expansion coefficients of one image at a time, the memory requirement for FFBsPCA is  $O(L^3)$  instead of  $O(L^4)$  in [7]. Therefore, the memory requirement for the new algorithm is significantly smaller. In addition, in Algorithm 2, radial eigenfunctions and steerable PCA expansion coefficients can also be efficiently computed in parallel for each angular index  $k$ .

## V. NUMERICAL EXPERIMENTS

We compare the running times of FFBsPCA, FBsPCA and traditional PCA, the latter does not include images' in-plane rotations for its computation. The algorithms are implemented in MATLAB on a machine with 12 cores, running at 2.3 GHz.

We first simulated  $n = 1000$  images with different size of compact support radius  $R$ , while the band limit is fixed at  $c = 1/2$ . For small  $R$ , since FFBsPCA performs polar Fourier transformation, it appears slightly slower than FBsPCA. However when  $R$  increases, FFBsPCA is computationally more efficient (see Tab. I). When  $R = 240$ , FFBsPCA becomes 25 times faster than FBsPCA. We also fixed the size of the image with  $R = 150$  and  $c = 1/2$  and varied the number of images  $n$ . Table II shows that the running time for FBsPCA and FFBsPCA grows linearly with  $n$  and FFBsPCA is the

$R$	PCA	FBsPCA	FFBsPCA
30	41.7	<b>0.9</b>	18.9
60	1460.6	<b>8.0</b>	23.8
90	$1.1 \times 10^4$	<b>31.7</b>	34.5
120	$5.0 \times 10^4$	89.6	<b>48.2</b>
150	$1.2 \times 10^5$	230.9	<b>96.7</b>
180	–	$1.2 \times 10^3$	<b>111.0</b>
210	–	$2.4 \times 10^3$	<b>139.2</b>
240	–	$4.1 \times 10^3$	<b>158.6</b>

TABLE I: Running time for different PCA methods (in seconds),  $n = 10^3$ ,  $c = 1/2$ , and  $R$  varies from 30 to 240.  $L = 2R$ .

$n$	PCA	FBsPCA	FFBsPCA
$1 \times 10^3$	2005	3.8	<b>1.6</b>
$2 \times 10^3$	2007	7.2	<b>2.6</b>
$4 \times 10^3$	2012	15.1	<b>5.3</b>
$8 \times 10^3$	2022	28.6	<b>10.5</b>
$1.6 \times 10^4$	2042	57.9	<b>19.9</b>

TABLE II: Running time for different PCA methods (in minutes). The number of images varies and each image is of size  $300 \times 300$  pixels,  $R = 150$ ,  $c = 1/2$  and  $L = 300$ .

fastest among the three methods. The running time for PCA is dominated by the eigendecomposition of the covariance matrix.

To show that our new algorithm can handle large datasets efficiently, we simulated a large dataset with  $10^5$  images of size  $300 \times 300$  pixels. The images consist entirely of Gaussian noise with mean 0 and variance 1. We assume that the compact support in image domain is  $R = 150$  and the band limit in Fourier domain is  $c = 1/2$ . In Table III, the total running time is divided into three parts: precomputation, Fourier-Bessel expansion (Algorithm 1), and steerable PCA (Algorithm 2). Fourier Bessel expansion took about 138 minutes, during which 86% of the time was spent on mapping images to polar Fourier grid, where we used the software package [19] downloaded from <https://www-user.tu-chemnitz.de/~potts/nfft/>. Numerical evaluation of the angular integration by 1D FFT and the radial integration by a direct method took 6% and 2% of the time respectively. The remaining 6% of the time were spent on saving the coefficients. Steerable PCA took 49 minutes, during which 26 minutes were spent on loading Fourier-Bessel expansion coefficients computed at the previous step.

In our third experiment, we simulated  $n = 10^5$  clean projection images from the reconstructed volume of human mitochondrial large ribosomal subunit downloaded from the

Steps	Time (min)
Precomputation	0.6
Fourier-Bessel Expansion	137.9
Steerable PCA	49.2
<b>Total</b>	<b>187.7</b>

TABLE III: Timing for FFBsPCA on a large dataset with  $n = 10^5$  images. Each image is of size  $300 \times 300$  pixels,  $R = 150$  and  $c = 1/2$ . We computed the full eigendecomposition in Algorithm 2.



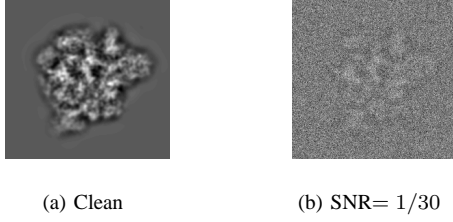


Fig. 4: Simulated projection images of the human mitochondrial large ribosomal subunit. Image size is  $240 \times 240$  pixels.

electron microscopy data bank [29]. The original volume in the data bank is of size  $320 \times 320 \times 320$  voxels. We preprocessed the volume such that the center of mass is at the origin and cropped out a volume of size  $240 \times 240 \times 240$  voxels that contains the particle. Each projection image is of size  $240 \times 240$  pixels. We simulated both the vanishing behavior of the CTF at low frequencies and the blurring effect by the Gaussian envelope of the CTF. This was done by convolving the images with the inverse Fourier transform of  $\min(\pi\lambda z f^2 + a, 1) \exp(-B f^2)$  where  $f$  is the frequency,  $\lambda$  is the wavelength of the electron beam,  $z$  is the defocus, and  $a$  is a phase of the CTF introduced by microscope. This stems from the analytic form of the CTF as  $\sin(\pi\lambda z f^2 + a) \exp(-B f^2)$ . For small  $f$ ,  $\sin(\pi\lambda z f^2 + a) \sim \pi\lambda z f^2 + a$ . We chose  $\lambda = 0.0197\text{\AA}$ ,  $z = 2.5\mu\text{m}$ ,  $a = 0.1\text{rad}$ , and  $B = 100\text{\AA}^2$  for simulation. The images (see Fig. 4a) were then corrupted by additive white Gaussian noise at SNR= 1/30, with noise variance  $\sigma^2 = 9$  (see Fig. 4b).

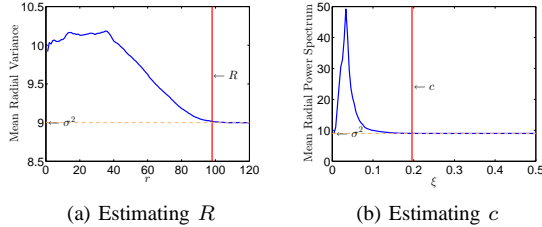


Fig. 5: Estimating  $R$  and  $c$  from  $n = 10^5$  simulated noisy projection images of human mitochondrial large ribosomal subunit. Each image is of size  $240 \times 240$  pixels. (a) Mean radial variance of the images. The curve levels off at about  $\sigma^2 = 9$  when  $r \geq 98$ . The radius of compact support is chosen at  $R = 98$ . (b) Mean radial power spectrum. The curve levels off at  $\sigma^2 = 9$  when  $\xi \geq 0.195$ . The band limit is chosen at  $c = 0.195$ .

We estimated the radius of compact support of the particle in real domain and the band limit in Fourier domain in the following way. We first subtracted the data mean from each image. Then we computed the 2D variance map of the dataset averaged in the angular direction to get a mean radial variance (see Fig. 5a). At large  $r$ , the mean radial variance levels off at 9, which corresponds to the noise variance. We subtracted

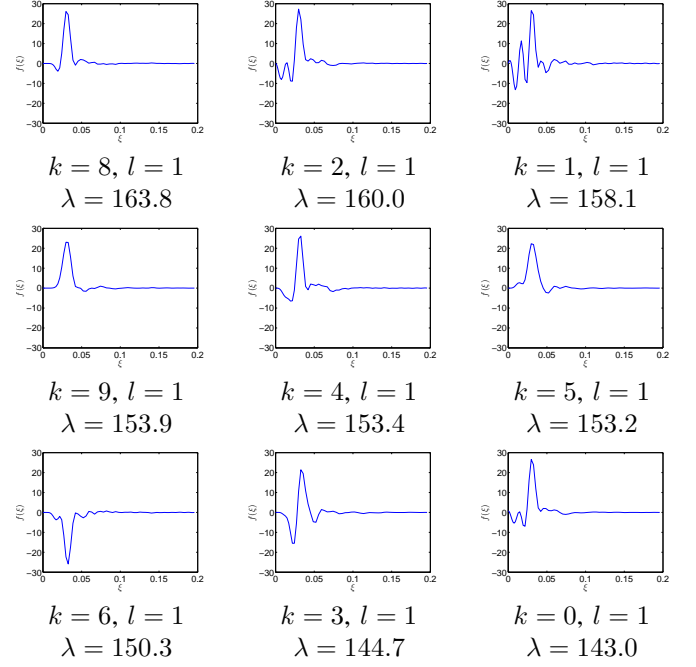


Fig. 6: FFBsPCA principal radial functions in Fourier domain. The dataset contains  $n = 10^5$  simulated human mitochondrial large ribosomal subunit projection images corrupted by additive white Gaussian noise with SNR= 1/30. Image size is  $240 \times 240$  pixels.  $R = 98$ ,  $c = 0.195$ . Each radial function is labeled with angular index  $k$ , radial order  $l$ , and eigenvalue  $\lambda$ .

the noise variance from the estimated mean radial variance and computed the cumulative variance by integrating the mean radial variance over  $r$  with a Jacobian weight  $rdr$ . The fraction of the cumulative variance reaches 99.9% at  $r = 98$ , and therefore  $R$  was chosen to be 98. In the Fourier domain, we computed the angular average of the mean 2D power spectrum. The curve in Fig. 5b also levels off at noise variance when  $\xi$  is large. We used the same method to compute the cumulative radial power spectrum. The fraction reaches 99.9% at  $\xi = 0.195$ , therefore the band limit is chosen to be  $c = 0.195$ .

The top nine radial eigenfunctions are shown in Fig. 6. Each radial function is indexed by  $k$  and  $l$ .  $k$  determines the angular Fourier mode and  $l$  is the order of the radial function within the same  $k$ . Taking the tensor product of the radial functions and their corresponding angular Fourier modes gives the two dimensional principal components in Fourier domain. It took 14 minutes in total to get the steerable PCA radial components and the associated expansion coefficients. In particular, Fourier-Bessel expansion coefficients were computed in 11 minutes and the steerable PCA took 3 minutes, during which about 2 minutes were spent on loading Fourier-Bessel expansion coefficients.

We computed the traditional PCA on the same dataset in real image domain (see Fig. 8) and it took 169 minutes. In order to compare the principal components computed by FFBsPCA with those computed by traditional PCA, we take the inverse Fourier transform of the FFBsPCA components. This is equivalent to computing the linear combination of  $\mathcal{F}^{-1}(\psi_c^{k,q})$  given



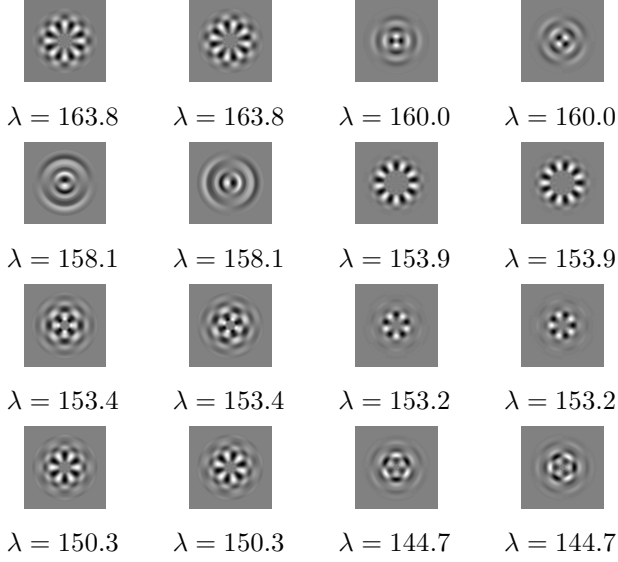


Fig. 7: FFBsPCA principal components (eigenimages in real domain) corresponding to Figure 6.

by Eq. (8). Those principal components are shown in Fig. 7. Some of the top sixteen principal components computed from traditional PCA and FFBsPCA look very similar, for example, the first three and the last four principal components (see Fig. 7 and Fig. 8). Because the gap between the eigenvalues of the traditional PCA is very small for the components in the middle two rows of Fig. 8, those components become degenerate and therefore look different from the corresponding components in Fig. 7.

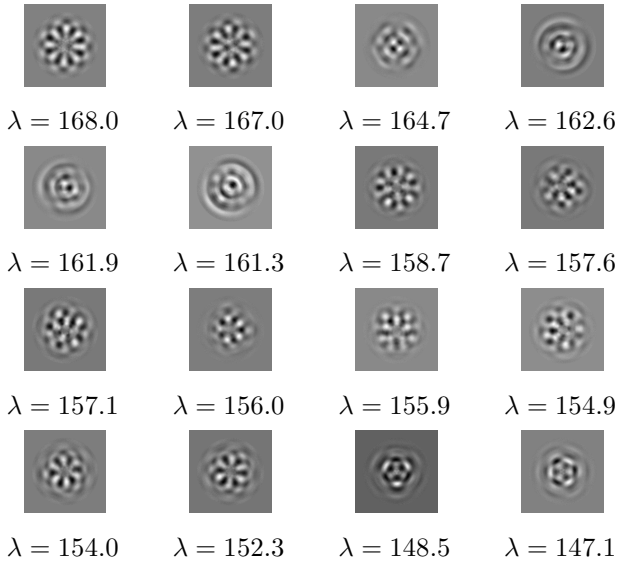


Fig. 8: Traditional PCA principal components in real image domain for the same dataset used in Figures 6 and 7.

In our simulation, each noisy projection image  $I$  is obtained by contaminating the clean image  $I_c$  with additive white Gaussian noise of variance  $\sigma^2 = 9$ . Since the transformation

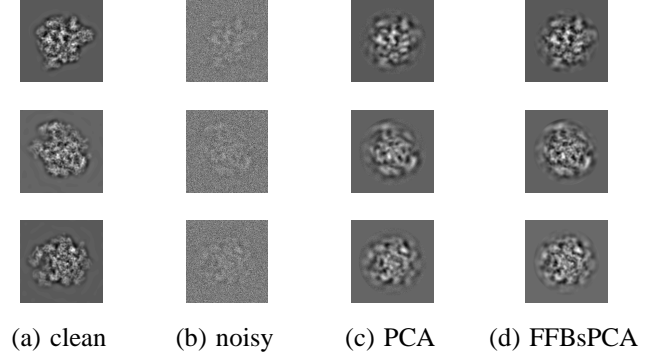


Fig. 9: Denoising simulated projection images from human mitochondrial large ribosomal subunit. The columns show (a) clean projection images, (b) noisy projection images with SNR= 1/30, (c) denoised projection images using traditional PCA, and (d) denoised images using FFBsPCA.

$T^*$  is nearly unitary, the coefficient matrices can be modeled approximately as  $A_c^{(k)} = A_c^{(k)} + \epsilon^{(k)}$ , where  $\epsilon^{(k)}$  is white Gaussian noise with variance  $\sigma^2$  and  $A_c^{(k)}$  is the coefficient matrix for the clean images. The covariance matrix  $C^{(k)}$  has eigenvalues  $\lambda_1^{(k)} \geq \lambda_2^{(k)} \geq \dots \geq \lambda_{p_k}^{(k)}$ . In the case when there is no signal, that is  $A_c^{(k)} = 0$ , all eigenvalues of the covariance matrix  $C^{(k)}$  converge to  $\sigma^2$  as  $n$  goes to infinity, while  $p_k$  is fixed. When  $A_c^{(k)} \neq 0$ , components with eigenvalues larger than  $\sigma^2$  correspond to the underlying clean signal. In the non-asymptotic regime of a finite number of images, the eigenvalues of the sample covariance matrix from white Gaussian noise spread around  $\sigma^2$ . The empirical density of eigenvalues can be approximated by the Marčenko-Pastur distribution with parameter  $\gamma_k$ , where  $\gamma_0 = \frac{p_0}{2n}$  and  $\gamma_k = \frac{p_k}{2n}$  for  $k > 0$  and the eigenvalues of  $C^{(k)}$  are supported on  $[\lambda_-^{(k)}, \lambda_+^{(k)}]$ , with  $\lambda_{\pm}^{(k)} = \sigma^2(1 \pm \sqrt{\gamma_k})^2$ . The components with eigenvalues larger than  $\lambda_+^{(k)}$  correspond to signal information beyond noise level. Therefore, with the estimated noise variance  $\hat{\sigma}^2$ , the components with eigenvalues

$$\lambda_l^{(k)} > \hat{\sigma}^2(1 + \sqrt{\gamma_k})^2, \quad l = 1, \dots, p_k \quad (36)$$

are selected. Various ways of selecting principal components from noisy data have been proposed. We refer to [30] for an automatic procedure for estimating the noise variance and the number of components beyond the noise level. For the simulated ribosomal subunit projections images, there are 966 steerable principal radial components above the threshold in Eq. (36), whereas considerably fewer principal components (391) with the traditional PCA were selected.

To first order approximation, when  $n \gg p_k$ , the noise simply shifts all eigenvalues upward by  $\sigma^2$  and this calls for soft thresholding of the sample covariance eigenvalues:  $(\lambda - \sigma^2)_+$ . To correct for the finite sample effect, we can apply more sophisticated shrinkage to the eigenvalues, such as the methods proposed in [31], [32]. Specifically, we applied the shrinkage method in [31] to the coefficients computed by both FFBsPCA and PCA. A few examples of denoised images are shown in Fig. 9. Because we were able to use more principal

components with FFBsPCA, we recovered finer details of the clean projection images, comparing the third and fourth columns in Fig. 9. We also computed the mean squared error

	MSE ( $10^{-5}$ )			PSNR (dB)		
	noisy	PCA	FFBsPCA	noisy	PCA	FFBsPCA
Image 1	52.7	1.10	<b>0.77</b>	2.27	19.06	<b>20.63</b>
Image 2	57.9	1.29	<b>0.96</b>	2.41	18.93	<b>20.23</b>
Image 3	55.6	1.17	<b>0.85</b>	3.22	19.99	<b>21.35</b>

TABLE IV: Denoising effects: MSE and PSNR of noisy images, denoised images using PCA, and denoised images using FFBsPCA.

(MSE) and Peak SNR (PSNR) to quantify the denoising effects in Table IV. Comparing with the traditional PCA, FFBsPCA reduced the MSE by more than 25% and increased the PSNR by over 1.3 dB. This experiment shows that FFBsPCA is an efficient and effective procedure for denoising large image datasets.

## VI. CONCLUSION

In this paper we presented a fast Fourier-Bessel steerable PCA method that reduces the computational complexity with respect to the size of the images so that it can handle larger images. The complexity of the new algorithm is  $O(nL^3 + L^4)$  compared with  $O(nL^4)$  of steerable PCA introduced in [7]. The key improvement is through mapping the images to polar Fourier grid using NUFFT and the evaluation of the Fourier-Bessel expansion coefficients by angular 1D FFT and accurate radial integration. FFBsPCA also reduces the memory requirement for parallel computation because only the radial part of the Fourier-Bessel basis is needed.

This work has been mostly motivated by its application to cryo-EM single particle reconstruction. Besides compression and denoising of the experimental images required for 2D class averaging [33] and common-line based 3D ab-initio modeling, FFBsPCA can also be applied in conjunction to Kam’s approach [34] that requires the covariance matrix of the 2D images [35]. The method developed here can also be extended to perform fast principal component analysis of a set of 3D volumes and their rotations. For this purpose, the Fourier-Bessel basis is replaced with the spherical-Bessel basis, and the expansion coefficients can be evaluated by performing the angular integration using a fast spherical harmonics transform [36] followed by radial integration.

Finally, we remark that the Fourier-Bessel basis can be replaced in our framework with other suitable bases, for example, the 2D prolate spheroidal wave functions (PSWF) on a disk [37]. The 2D prolates also have a separation of variables form which makes them convenient for steerable PCA. A possible advantage of using 2D prolates is that they are optimal in terms of the size of their support.

## ACKNOWLEDGMENT

This research was supported by Award Number R01GM090200 from the NIGMS (A. S. and Y. S.), Award Number LTR DTD 06-05-2012 from the Simons

Foundation (A. S.), and Grant Number 578/14 from the Israel Science Foundation (Y. S.). The authors would like to thank Leslie Greengard, Michael O’Neil, and Alex Townsend for valuable discussions.

## REFERENCES

- [1] M. van Heel and J. Frank, “Use of multivariate statistics in analysing the images of biological macromolecules,” *Ultramicroscopy*, vol. 6, no. 2, pp. 187–194, 1981.
- [2] J. Frank, *Three-Dimensional Electron Microscopy of Macromolecular Assemblies: Visualization of Biological Molecules in Their Native State*. Oxford, 2006.
- [3] R. Hilai and J. Rubinstein, “Recognition of rotated images by invariant Karhunen-Loève expansion,” *J. Opt. Soc. Am. A.*, vol. 11, no. 5, pp. 1610–1618, 1994.
- [4] P. Perona, “Deformable kernels for early vision,” *IEEE Trans. Pattern Anal. Mach. Intell.*, vol. 17, no. 5, pp. 488–499, 1995.
- [5] M. Uenohara and T. Kanade, “Optimal approximation of uniformly rotated images: Relationship between Karhunen-Loève expansion and discrete cosine transform,” *IEEE Trans. Image Process.*, vol. 7, no. 1, pp. 116–119, 1998.
- [6] C. Ponce and A. Singer, “Computing steerable principal components of a large set of images and their rotations,” *IEEE Trans. Image Process.*, vol. 20, no. 11, pp. 3051–3062, 2011.
- [7] Z. Zhao and A. Singer, “Fourier-Bessel rotational invariant eigenimages,” *J. Opt. Soc. Am. A.*, vol. 30, no. 5, pp. 871–877, 2013.
- [8] C. Vonesch, F. Stauber, and M. Unser, “Design of steerable filters for the detection of micro-particles,” in *Proceedings of the 10th IEEE International Symposium on Biomedical Imaging (ISBI 2013): From Nano to Macro*, 2013, pp. 934 – 937.
- [9] R. Lenz, “Group-theoretical model of feature extraction,” *J. Opt. Soc. Am. A*, vol. 6, pp. 827–834, 1989.
- [10] —, “Group invariant pattern recognition,” *Pattern Recognition*, vol. 23, pp. 199–217, 1990.
- [11] —, “Steerable filters and invariant recognition in spacetime,” in *Proceedings of the International Conference of Acoustics, Speech and Signal Processing*. IEEE Computer Science Press, 1998, pp. 2737–2740.
- [12] R. Lenz, T. H. Bui, and Hernández-Andrés, “Group theoretical structure of spectral spaces,” *J. Math. Imaging Vis.*, vol. 23, pp. 297–313, 2005.
- [13] R. Lenz, “Investigation of receptive fields using representations of the dihedral groups,” *J. Vis. Commun. Image Represent.*, vol. 6, no. 3, pp. 209–277, 1995.
- [14] M. Jogan, E. Zagar, and A. Leonardis, “Karhunen-Loève expansion of a set of rotated templates,” *IEEE Trans. Image Process.*, vol. 12, no. 7, pp. 817–825, 2003.
- [15] A. Klug and R. A. Crowther, “Three-dimensional image reconstruction from the viewpoint of information theory,” *Nature*, vol. 238, pp. 435–440, 1972.
- [16] A. Dutt and V. Rokhlin, “Fast Fourier Transforms for Nonequispaced Data,” *SIAM Journal on Scientific Computing*, vol. 14, no. 6, pp. 1368–1393, 1993.
- [17] J. A. Fessler and B. P. Sutton, “Nonuniform fast Fourier transforms using min-max interpolation,” *IEEE Trans. Signal Process.*, vol. 51, no. 2, pp. 560 – 574, 2003.
- [18] L. Greengard and J. Lee, “Accelerating the Nonuniform Fast Fourier Transform,” *SIAM Review*, vol. 46, no. 3, pp. 443–454, 2004.
- [19] M. Fenn, S. Kunis, and D. Potts, “On the computation of the polar FFT,” *Appl. Comput. Harm. Anal.*, vol. 22, pp. 257–263, 2007.
- [20] M. O’Neil, F. Woolfe, and V. Rokhlin, “An algorithm for the rapid evaluation of special function transforms,” *Appl. Comput. Harmon. Anal.*, vol. 28, pp. 203–226, 2010.
- [21] A. Townsend, “A fast analysis-based discrete Hankel transform using asymptotic expansions,” [arxiv.org/abs/1501.01652](https://arxiv.org/abs/1501.01652), 2015.
- [22] G. N. Watson, *Theory of Bessel Functions*. Cambridge, 1944.
- [23] M. Abramowitz and I. A. Stegun, *Handbook of Mathematical Functions with Formulas, Graphs, and Mathematical Tables*, ser. Applied Mathematics Series. US Natuional Bureau of Standards, 1964, vol. 55.
- [24] F. W. J. Olver, “A further method for the evaluation of zeros of Bessel functions and some new asymptotic expansions for zeros of functions of large order,” *Mathematical Proceedings of the Cambridge Philosophical Society*, vol. 47, pp. 699–712, 1951.
- [25] Á. Elbert, “Some recent results on the zeros of Bessel functions and orthogonal polynomials,” *J. Comput. Appl. Math.*, vol. 133, no. 1-2, pp. 65–83, 2001.

- [26] S. Breen, "Uniform upper and lower bounds on the zeros of Bessel functions of the first kind," *J. Math. Anal. Appl.*, vol. 196, pp. 1–17, 1995.
- [27] W. H. Press, B. P. Flannery, S. A. Teukolsky, and W. T. Vetterling, *Numerical recipes in FORTRAN 77: The art of scientific computing*. Cambridge University Press, 1986.
- [28] P. A. Rattey and A. G. Lindgren, "Sampling the 2-D Radon transform," *IEEE Trans. Acoust., Speech, Signal Processing*, vol. ASSP-29, no. 5, pp. 994–1002, 1981.
- [29] A. Brown, A. Amunts, X. Bai, Y. Sugimoto, P. C. Edwards, G. Murshudov, S. H. W. Scheres, and V. Ramakrishnan, "Structure of the large ribosomal subunit from human mitochondria," *Science*, vol. 346, no. 6210, pp. 718–722, 2014.
- [30] S. Kritchman and B. Nadler, "Determining the number of components in a factor model from limited noisy data," *Chemometr. Intell. Lab.*, vol. 94, pp. 19–32, 2008.
- [31] A. Singer and H.-T. Wu, "Two-Dimensional tomography from noisy projections taken at unknown random directions," *SIAM J. Imaging Sci.*, vol. 6, no. 1, pp. 136–175, 2013.
- [32] D. L. Donoho, M. Gavish, and I. M. Johnstone, "Optimal shrinkage of eigenvalues in the spiked covariance model," [arxiv.org/abs/1311.0851](http://arxiv.org/abs/1311.0851), 2014.
- [33] Z. Zhao and A. Singer, "Rotationally invariant image representation for viewing direction classification in cryo-em," *J. Struct. Biol.*, vol. 186, no. 1, pp. 153–166, 2014.
- [34] Z. Kam, "The reconstruction of structure from electron micrographs of randomly oriented particles," *J. theor. Biol.*, vol. 82, pp. 15–39, 1980.
- [35] T. Bhamre, T. Zhang, and A. Singer, "Orthogonal matrix retrieval in cryo-electron microscopy," in *Proceedings of the 12th IEEE International Symposium on Biomedical Imaging (ISBI 2015)*, 2015, also available at <http://arxiv.org/abs/1412.0494>.
- [36] V. Rokhlin and M. Tygert, "Fast algorithms for spherical harmonic expansions," *SIAM J. Sci. Comput.*, vol. 27, no. 6, pp. 1903–1928, 2006.
- [37] D. Slepian, "Prolate spheroidal wave functions, Fourier analysis, and uncertainty–IV: extensions to many dimensions, generalized prolate spheroidal wave functions," *Bell System Technical Journal*, vol. 43, pp. 3009–3057, 1964.